Satellite Image-Based Estimation of Urban Air Pollution in Tehran Under Climate Change Using Digital Image Processing for Air Quality Monitoring

Amir Hossein Sabzevari[1], Mahmood Hajiani[*2,3], Raziyeh Azizi[4]

1- M.Sc. student of Civil Eng., Faculty of Civil Engineering, University of Tehran, Iran

2- Associate Professor, Department of Civil Engineering, Faculty of Engineering, University of Birjand, Iran. Orcid.org/0000-0002-3612-2339

3- Department of Research Group of Drought and Climate Change, University of Birjand, Iran.

4- PhD candidate in Environmental Eng., Department of Environmental Engineering, Faculty of Natural Resources and Environment, University of Birjand, Iran.

***Corresponding Author:** hajiani@birjand.ac.ir

Abstract

Urban air pollution is a major global health threat, exacerbated by climate change through altered temperature inversions, boundary layer dynamics, and pollutant dispersion. Ground-based monitoring networks are costly and spatially limited. This study assesses the feasibility of estimating the Air Quality Index (AQI) from Google Earth satellite imagery of Tehran using three digital image processing methods in MATLAB. Seven cloud-free satellite images acquired between July 2022 and April 2024 (AQI range: 64-172) were analyzed. Three image-derived features were correlated with AQI: (1) pixel intensity standard deviation from normalized grayscale histograms, (2) Pearson cross-correlation coefficients relative to a clean-day reference, and (3) mean edge pixel density from Canny edge detection. Linear regression models were trained on five images and validated on two withheld test images. Pixel standard deviation showed a strong inverse relationship with AQI ($R^2 = 0.82$; regression slope: 1160.98 ± 312.4, intercept: 361.71 ± 75.3), with test errors of 1.25% and 29.66%. Canny edge detection mean density yielded $R^2 = 0.80$ (slope: 925.41 ± 268.7, intercept: 319.35 ± 64.9) with balanced errors of 10.11% and 12.81%, indicating greater seasonal robustness. Cross-correlation confirmed that pollution distorts structural image similarity, but showed limited predictive consistency across seasons due to illumination variability. The results suggest that freely available optical satellite imagery may encode air quality-relevant information accessible through simple image operations, without specialized sensors or atmospheric correction.

Keywords: AQI estimation, Dust; Remote sensing, Edge Detection, Tehran.

Introduction

Climate change intensifies urban air pollution through multiple mechanisms. Urban air pollution represents one of the most serious environmental and public health crises of the current era.(Pato et al., 2025). Approximately 99% of the global population breathes air that does not meet WHO-recommended quality thresholds, with urban residents bearing a disproportionate burden of disease (World Health Organization, 2022). Key pollutants, including fine particulate matter (PM2.5 and PM10)(Rybarczyk et al., 2025)sulfur dioxide (SO_2), nitrogen dioxide (NO_2), ground -level ozone (O_3), and carbon monoxide (CO) are strongly linked to cardiovascular disease, respiratory illness, neurological disorders, and premature mortality(Lelieveld et al., 2015; Burnett et al., 2018; Farzaneh et al., 2024).

An additional dimension of growing concern is the interaction between air pollution and climate change. Rising temperatures associated with global warming alter the chemistry and transport of atmospheric pollutants in several interconnected ways (Zhu et al., 2019). Higher temperatures accelerate the photochemical formation of ground-level ozone. Urban heat island effects intensify near-surface temperature inversions that trap particulate matter close to the ground. Changes in wind patterns and precipitation frequency affect the vertical mixing and washout of aerosols. In basin-shaped cities such as Tehran, where topographic enclosure already limits dispersion, climate-driven changes in atmospheric dynamics are expected to exacerbate pollution episodes in frequency and severity (Lim et al., 2020; Shahbazi et al., 2016). These feedback mechanisms mean that air quality monitoring systems must not only be robust today, but also scalable and adaptable to a future climate characterized by more extreme weather variability. It is important to distinguish between two separate pathways through which climate change influences this study. First, climate change directly affects air quality by modifying atmospheric processes

Pre-publication version

such as pollutant formation, transport, dispersion, and accumulation. Second, climate change may indirectly affect the performance of image-based monitoring approaches by altering environmental conditions that influence image appearance, including solar illumination patterns, vegetation dynamics, atmospheric humidity, and surface reflectance. Therefore, future monitoring systems must be capable of adapting not only to changing pollution conditions but also to changing image acquisition environments.

The Air Quality Index (AQI) is the internationally standardized tool for communicating pollution levels to the public. However, the dense sensor networks required for spatially continuous AQI monitoring are expensive to install and maintain, restricting comprehensive coverage in lower-income regions and in cities undergoing rapid expansion (Kumar et al., 2015). This limitation has driven substantial research into cost-effective alternative monitoring strategies capable of providing spatial coverage without the overhead of physical sensor deployments.

Remote sensing via satellite has emerged as a powerful complement to ground-based monitoring networks. (Kaufman et al., 2002, Levy et al., 2010). Satellite platforms such as MODIS, Sentinel-2, and Landsat provide regular, spatially extensive imagery that has been used to derive aerosol optical depth (AOD), a well-established proxy for column-integrated particulate loading. (Van Donkelaar et al., 2010). Several studies have demonstrated reasonable accuracy in converting AOD to near-surface PM2.5 concentrations. (Xiao et al., 2017), though these approaches require access to specialized multispectral products and complex atmospheric correction pipelines.

A parallel and less explored avenue involves analysis of conventional visible spectrum satellite imagery, including freely accessible platforms such as Google Earth, using standard digital image processing techniques. The physical rationale is straightforward: atmospheric aerosols scatter and absorb solar radiation, reducing the contrast, sharpness, and spectral richness of images acquired through a polluted atmosphere.(Narasimhan & Nayar, 2002, He et al., 2010). This connection between image clarity and pollution has motivated the application of histogram statistics, image cross-correlation, and edge detection as candidate pollution proxies.(Narasimhan & Nayar, 2002, Li et al., 2017). Fig. 1 illustrates this effect conceptually: in a hazy, polluted scene, the contrast between objects is visibly reduced relative to clear conditions.



Fig 1. Illustrative example of the visual impact of air pollution on image clarity. In highly polluted conditions, atmospheric particulates scatter light and suppress contrast, reducing the distinctness of objects in the scene (Shi et al., 2020).

The effect shown in Fig. 1 is also reflected in the pixel intensity distribution (histogram) of polluted versus clean satellite images. Fig. 2 shows Google Earth images of two contrasting cities, Delhi, India (a severely polluted megacity) and Babolsar, Iran (a comparatively clean coastal city), together with their respective grayscale histograms. The Delhi histogram is tightly concentrated at mid-range intensities, indicating low spatial contrast consistent with aerosol-induced attenuation, whereas the Babolsar histogram is broadly distributed, reflecting high scene clarity.

Pre-publication version

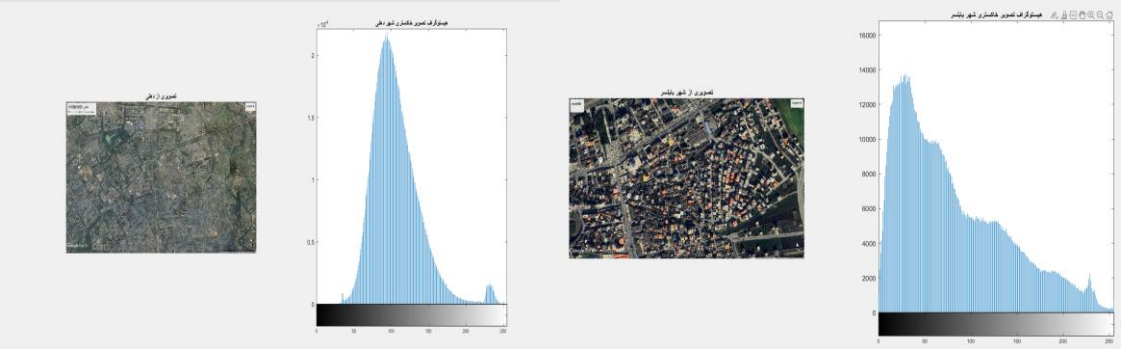


Fig 2. Satellite images and corresponding grayscale histograms for Delhi, India (AQI 300; left) and Babolsar, Iran (low AQI; right). The compressed histogram of Delhi reflects reduced spatial contrast caused by heavy aerosol loading, while the broad histogram of Babolsar indicates a clear atmosphere and rich scene detail.

Prior studies have leveraged this principle in various forms. Liu et al. (Liu et al., 2016) applied color histogram analysis to sky imagery to classify pollution levels, showing that pixel intensity distributions shift systematically with PM concentrations. Palvanov and Cho (Palvanov & Cho, 2019) developed a convolutional neural network for visibility estimation from single images, achieving accuracy comparable to instrumented measurements. Joans and Pavithra (Joans & Pavithra, 2017) demonstrated that edge density in traffic camera images decreases in foggy or polluted conditions, a finding that directly motivates the edge detection approach adopted in the present study. Liu et al. (2016) reviewed image processing methods for urban air pollution monitoring, including AOD retrieval from satellite multispectral data and webcam-based online systems.

Research on remote sensing of urban air quality has advanced along several parallel trajectories. The most established line of work uses aerosol optical depth (AOD) retrieved from multispectral satellite platforms, principally MODIS Terra/Aqua, MISR, and the newer MAIAC product, as a proxy for near-surface PM2.5. Gupta et al. (2006) demonstrated AOD PM2.5 correlations for global cities, and van Donkelaar et al. (2010) produced global annual PM2.5 maps by coupling satellite AOD with chemical transport model simulations. More recently, Xiao et al. (2017) generated high-resolution daily PM2.5 estimates for the Yangtze River Delta using MAIAC AOD.(Xiao et al., 2017). A second research stream exploits visible spectrum ground - level cameras. Liu et al. (2016) applied pixel intensity and color histogram analysis to sky images and showed that histogram shape shifts systematically with PM concentration. Joans and Pavithra (2017) demonstrated that edge density in traffic camera images decreases under foggy or polluted conditions, directly motivating the approach adopted here.(Joans & Pavithra, 2017). Palvanov and Cho (2019) trained a convolutional neural network (VisNet) for visibility estimation from single images, achieving accuracy comparable to instrumented sensors (Palvanov & Cho, 2019). A third line of work addresses image dehazing: Narasimhan and Nayar (2002) formalized the atmospheric scattering model underpinning all image-based pollution indicators.(Narasimhan & Nayar, 2002), while He et al. (2010) extended this framework to single image haze removal using the dark channel prior(He et al., 2010).

Despite these contributions, studies that (a) use freely accessible, non calibrated optical satellite imagery, (b) compare multiple image processing features under a controlled AQI range, and (c) explicitly discuss climate change implications for monitoring robustness are essentially absent from the literature.

The novelty of the present study lies in three respects. First, whereas prior image-based air quality studies have predominantly used either ground-level cameras or calibrated multispectral satellite sensors, this work applies three complementary image processing methods directly to freely accessible, consumer grade Google Earth optical imagery, making the pipeline technically accessible to practitioners without specialized remote sensing infrastructure. Second, the three methods are evaluated comparatively on the same controlled dataset spanning a defined AQI range, allowing a direct head-to-head assessment of their predictive capacity and seasonal robustness, a form of comparative evaluation rarely conducted in the existing literature. Third, the results are interpreted explicitly in the context of climate change: the study discusses how projected shifts in seasonal temperature, insolation, and boundary layer dynamics may affect the reliability of each method, situating this technical work within a broader climate adaptation framework.

The scope of this research is deliberately constrained: three specific image processing features (pixel intensity standard deviation, Pearson cross-correlation, and Canny edge density) applied to seven visible spectrum satellite images of a single fixed location in Tehran, covering AQI values between 64 and 172 over a 22-month observation window. The study does not attempt to develop an operational air quality

Pre-publication Version

monitoring product; rather, it constitutes a methodological feasibility test intended to assess whether meaningful AQI-relevant information exists within this class of imagery and to identify which feature extraction approach is most robust to seasonal illumination variability. Findings are intended to inform the design of more extensive follow on studies, not to provide production-ready predictions.

Before proceeding, it is important to acknowledge the inherent limitations of this research. The dataset comprises only seven satellite images, which limits statistical inference and makes it impossible to claim that the regression models are generalizable beyond the specific site and AQI range examined. All images are confined to the visible spectrum, which is vulnerable to confounding by seasonal solar geometry, vegetation phenology, and cloud shadow effects. Image acquisition times were not standardized across dates, introducing additional illumination variability. AQI values represent citywide daily averages that may not perfectly reflect the atmospheric column directly above the specific satellite image footprint. These constraints mean that the findings should be treated as exploratory and hypothesis-generating rather than definitive.

This study addresses these gaps with three specific objectives: (i) to assess whether pixel intensity standard deviation, image cross correlation, and Canny edge detection mean density are correlated with AQI in a dataset of seven satellite images of Tehran spanning AQI 64 -172; (ii) to derive and validate simple linear regression models linking these features to AQI; and (iii) to discuss the performance, limitations, and climate change implications of each approach. Tehran was selected as the study site because it consistently ranks among the most polluted major cities in Asia, and because its topographic enclosure makes it particularly vulnerable to climate-driven exacerbation of pollution events(Naddafi et al., 2012, Shahbazi et al., 2016).

Materials and Methods

Air Quality Index (AQI)

The Air Quality Index is a dimensionless scale used to report ambient air quality based on concentrations of key regulated pollutants. Sub-indices are calculated separately for each pollutant using a piecewise linear interpolation (Equation 1):

$$I_P = \frac{I_{Hi} - I_{L0}}{BP_{Hi} - BP_{L0}}\left(C_p - BP_{L0}\right) + I_{L0} \quad (1)$$

where I_p is the sub-index for pollutant p; C_p is the rounded measured concentration; BP_{Hi} and BP_{Lo} are the upper and lower concentration breakpoints bounding C_p; and I_{Hi} and I_{Lo} are the corresponding AQI index values. The reported AQI equals the maximum subindex across all measured pollutants. Table 1 summarises AQI categories and health implications.

AQI was selected as the target variable in this study rather than PM2.5 concentration or aerosol optical depth (AOD) for three reasons. First, the AQI is a composite index that captures the dominant pollutant on any given day, making it a more holistic proxy for total optical degradation of the atmosphere than any single species metric. In Tehran, the dominant pollutant shifts seasonally between PM2.5 (winter) and ozone (summer), so a PM2.5-only target would systematically mislabel summer episodes. Second, AOD retrieval requires radiometrically calibrated multispectral data and atmospheric correction; neither is available for Google Earth imagery, which is a compressed visual product. Third, AQI values are publicly reported daily by urban monitoring networks worldwide, making the approach directly scalable to data limited cities a key practical motivation of the study. (Gupta et al., 2006, Liu et al., 2016).

Table 1. AQI categories and associated health risk levels.

AQI Range	Category	Color	Health Implications
0–50	Good	Green	Minimal risk
51–100	Moderate	Yellow	Acceptable; sensitive groups may be affected
101–150	Unhealthy for Sensitive Groups	Orange	Sensitive groups at risk
151–200	Unhealthy	Red	Everyone may experience effects

Pre-publication Version

201–300	Very Unhealthy	Purple	Health alert
301–500	Hazardous	Maroon	Emergency conditions

Pixel Intensity Statistics and Image Histograms

A digital image is a two dimensional matrix of discrete intensity values. In grayscale representation, each pixel carries a value from 0 (black) to 255 (white) in 8-bit encoding. The image histogram describes the frequency distribution of these values across the entire image (Gonzalez, 2009). In a clear sky image with rich spatial detail, the histogram spans a wide range of intensities, reflecting the diversity of urban surface materials: rooftops, roads, vegetation, water. When aerosols increase, they scatter and absorb solar radiation, attenuating the contrast between adjacent surfaces and compressing the histogram toward midrange values (Narasimhan & Nayar, 2002, Pizer et al., 1987). The standard deviation (σ) of pixel intensities quantifies this compression (equation (2)):

$$\sigma = \sqrt{[\,(1/N)\,\Sigma_i\,(x_i - \mu)^2\,]} \tag{2}$$

where N is the total pixel count, x_i is the intensity of pixel i, and μ is the mean intensity. A lower σ indicates a flatter, uniform image, a signature of pollution-induced contrast attenuation(Pizer et al., 1987) .

Image Cross Correlation

The degree of structural similarity between two same size images A and B can be quantified by the Pearson cross-correlation coefficient r. This is computed as shown in Equation (3):

$$\frac{\sum(x_i - \bar{x})\,(y_i - \bar{y})}{\sqrt{\sum(x_i - \bar{x})^2\,\sum(y_i - \bar{y})^2}} \tag{3}$$

Where x_i and y_i represent pixel intensities of images A and B, respectively, and $\bar{x}$, $\bar{y}$ denote their means.
The coefficient r ranges from -1 to +1. When a target image closely resembles the reference (taken on a clean day), r approaches 1. As pollution alters scene appearance through haze and reduced contrast, r decreases. Analyzing correlation across multiple spectral channels (R, G, and B) can reveal whether pollutants differentially affect certain wavelength bands.(Xu et al., 2022).

Canny Edge Detection

Edge detection identifies boundaries between image regions with distinct intensity levels, corresponding to physical boundaries between objects in the scene. The Canny algorithm is the most widely adopted edge detector due to its optimal noise suppression and single response per edge property (Canny, 1986). It applies Gaussian smoothing, gradient computation (using Sobel operators), non-maximum suppression, and double threshold hysteresis to produce a binary edge map in which white pixels (value = 1) mark edge locations and black pixels (value = 0) mark non-edge regions.
In a clear atmosphere, the distinct intensity boundaries between urban surfaces produce a dense, well defined edge map. Atmospheric particulates scatter light and reduce local contrast, suppressing edge detection and lowering the mean pixel value of the binary edge map (Joans & Pavithra, 2017). This mean edge density the fraction of pixels classified as edges, therefore serves as a proxy for scene clarity and, by extension, for air quality.

Study Site and Image Acquisition

The study site is a fixed geographic location in central Tehran, Iran (approximately 35.68° N, 51.39° E). Tehran is one of the most persistently polluted capitals in Asia, with frequent AQI exceedances attributable to heavy vehicular emissions, industrial activity, and the topographic confinement of the Alborz mountain range to the north (Naddafi et al., 2012; Shahbazi et al., 2016). Under projected climate change scenarios, reductions in ventilation from westerly winds and increases in summer temperature inversions are expected to intensify pollution episodes, making Tehran an important and representative test site for scalable monitoring methods (Lim et al., 2020). Tehran has a semi-arid continental climate with a mean annual temperature of approximately 17.5°C, a mean January minimum of approximately 1-3°C, and a mean July

Pre-publication Version

maximum of approximately 36-38°C (Shahbazi et al., 2016). The large seasonal temperature range exceeding 30°C between winter and summer extremes is directly relevant to the interpretation of image variability in this study, as solar elevation angles differ markedly between winter and summer, producing substantial interseasonal differences in image illumination that are independent of air quality.

Seven cloud-free satellite images were obtained from Google Earth Pro for the same geographic location in Tehran between July 2022 and April 2024. For each image date, the corresponding daily Air Quality Index (AQI) value was obtained from the Tehran Air Quality Monitoring Network. Each satellite image was paired with the AQI reported for the same calendar day to ensure temporal consistency between image observations and air quality measurements. The resulting dataset covered AQI conditions ranging from 64 to 172.

All images were exported at a consistent spatial scale and orientation. Fig. 3 displays the seven satellite images alongside their acquisition dates and AQI values. Visual differences in image appearance across pollution levels particularly the progressive loss of surface contrast and color saturation at higher AQI are apparent even from direct visual inspection.

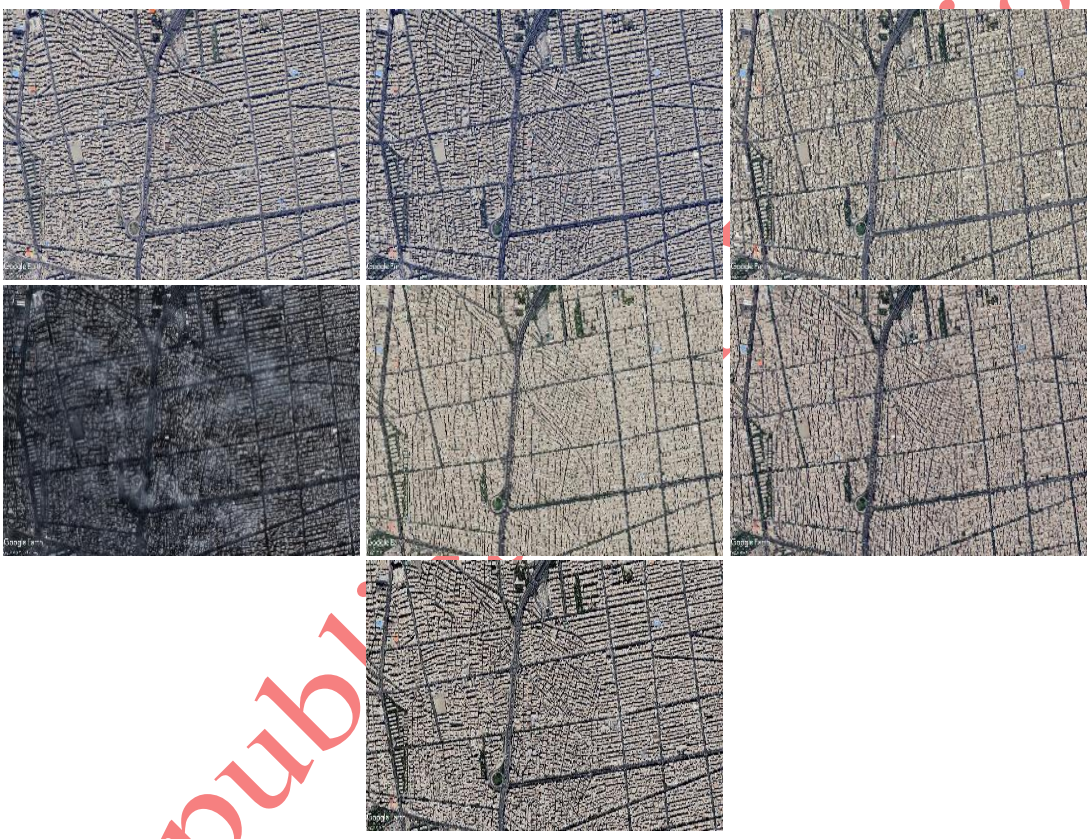


Fig 3. The seven Google Earth satellite images of the study location in Tehran used in this study. Top row (left to right): T1 (AQI = 64, Apr 2024), T2 (AQI = 73, Sep 2023), T3 (AQI = 86, Jun 2023). Middle row: T4 (AQI = 172, Dec 2022), T5 (AQI = 162, Jul 2022), T6 (AQI = 109, Aug 2022). Bottom: T7 (AQI = 78, Sep 2022). Progressive loss of image contrast and spatial detail is visually apparent at higher AQI values.

Corresponding AQI data and individual pollutant sub-indices were obtained from the Tehran Air Quality Monitoring Network for the date of each image. Meteorological conditions (temperature and relative humidity) were also recorded. The complete dataset is summarized in Table 2.

Table 2. Dataset: satellite image acquisition dates, AQI values, individual pollutant sub-indices, and meteorological conditions for Tehran.

Image	Date	AQI	$PM_{2.5}$	PM_{10}	SO_2	NO_2	O_3	CO	Temp (°C)	RH (%)
T1	04 Apr 2024	64	64	49	17	64	42	29	24	12.15
T2	30 Sep 2023	73	73	56	19	52	35	36	26	14.61
T3	03 Jun 2023	86	70	49	10	61	86	21	32	13.85

Pre-publication

T4	15 Dec 2022	172	172	113	101	78	6	56	11	46.59
T5	16 Jul 2022	162	92	63	27	81	162	35	33	12.18
T6	04 Aug 2022	109	77	56	10	82	109	25	36	11.92
T7	04 Sep 2022	78	78	61	22	71	68	35	32	8.89

Image Preprocessing

All images were loaded into MATLAB (R2023a) using the imread function and converted to grayscale using rgb2gray, which applies a luminance weighted combination of RGB channels (0.2989R + 0.5870G + 0.1140B) (Poynton, 2012). Grayscale conversion reduces dimensionality while preserving the spatial intensity structure relevant to pollution induced visual changes. For the cross correlation analysis, both the grayscale matrix and individual RGB channel matrices were processed separately. All computations used standard MATLAB built-in functions to ensure reproducibility.

Feature Extraction Methods

Pixel Intensity Standard Deviation

Each grayscale image was normalized to (World Health Organization, 2022) by dividing by 255. The standard deviation of the entire pixel matrix was computed using the std2 function. Lower σ values correspond to more uniform, lower contrast images characteristic of higher pollution levels.

Image Cross Correlation

Image T1 (AQI = 64), which exhibited the lowest AQI value among all observations, was selected as the reference image. The rationale for this choice was that T1 represented the clearest atmospheric conditions available within the dataset and therefore provided the most suitable baseline for assessing pollution-related degradation of image quality. It should be noted that an AQI of 64 falls within the 'Moderate' category (51-100) per EPA classification, meaning T1 cannot be treated as a truly clean air reference. The use of a moderately polluted image as a reference introduces a systematic bias into the cross-correlation analysis: all computed correlation values represent similarity to a reference that is itself somewhat aerosol affected rather than to a hypothetical pristine scene. This is a recognized limitation of the cross-correlation approach in small datasets and is one reason why correlation values, even for relatively clean images such as T7 (AQI = 78), are not as interpretable as they would be with a verified clean-day baseline. For future work, composite clear-day images derived from long-term averages are recommended. The corr2 function was applied to compute the 2D Pearson cross-correlation coefficient between the reference and each of the seven target images, evaluated over the grayscale matrix and each of the three RGB channels independently.

Canny Edge Detection and Mean Edge Density

The edge function with the 'Canny' method was applied to each normalized grayscale image. The resulting binary edge map was converted to a double-precision range (World Health Organization, 2022). The arithmetic mean of this map, representing the fraction of pixels identified as edges, was computed using mean2. A higher mean edge density indicates a clearer scene; a lower value reflects pollution-induced suppression of spatial contrast.

Regression Modeling and Validation

Ordinary least squares linear regression models were fitted separately for the standard deviation and edge density features using the five chronologically earliest observations (T1-T5) as the training set. The two remaining observations (T6, T7) served as a withheld test set. Model fit was evaluated by R^2, and predictive accuracy on the test set was assessed by relative prediction error (|predicted observed| / observed × 100%). Cross-correlation coefficients were analyzed descriptively, as their relationship with AQI was substantially confounded by seasonal scene variation.

Results and Discussion

Pixel Intensity Histograms

Fig. 4 presents the edge detected thumbnails and grayscale histograms for all seven Tehran images. The histograms provide direct visual evidence of the compression effect: images acquired on high AQI days (T4 with AQI = 172, T5 with AQI = 162) show histograms that peak sharply at low intensity values, indicating a predominantly dark, low-contrast scene. Images acquired under moderate to clean conditions (T1 with

Pre-publication Version

AQI = 64, T7 with AQI = 78) show broader, more evenly distributed histograms. This behavior is consistent with the physical mechanism described in Section 2.2, whereby atmospheric aerosols scatter and attenuate incoming and reflected radiation, reducing scene visibility and suppressing contrast between adjacent surface features. As visibility decreases, the range of detectable pixel intensities becomes narrower, resulting in the compressed histogram distributions observed for images acquired under more polluted conditions.

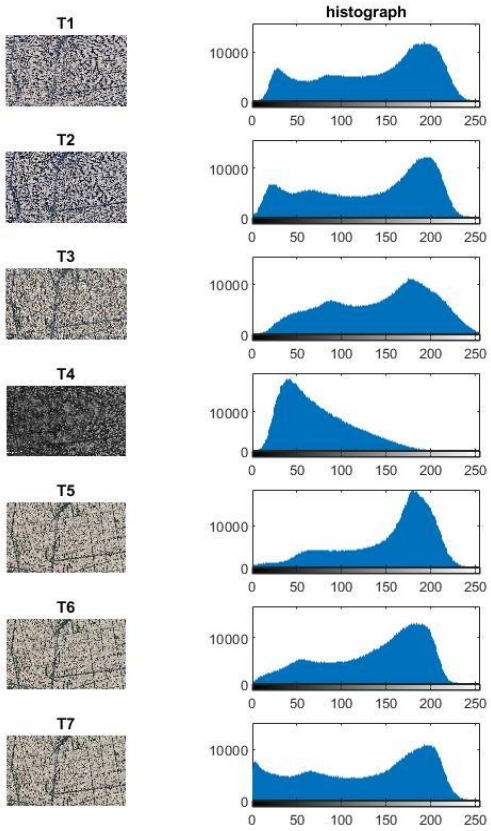


Fig 4. Edge detected thumbnails (left) and grayscale pixel intensity histograms (right) for the seven Tehran satellite images (T1-T7). Images with higher AQI values show compressed, sharply peaked histograms at low intensity levels, reflecting reduced scene contrast due to aerosol induced light scattering.

Fig. 5 presents the normalized (World Health Organization, 2022) pixel intensity histograms stacked for all seven images, facilitating direct comparison. The shift of the histogram peak toward lower values as AQI increases is consistently visible across the dataset.

Pre-print version

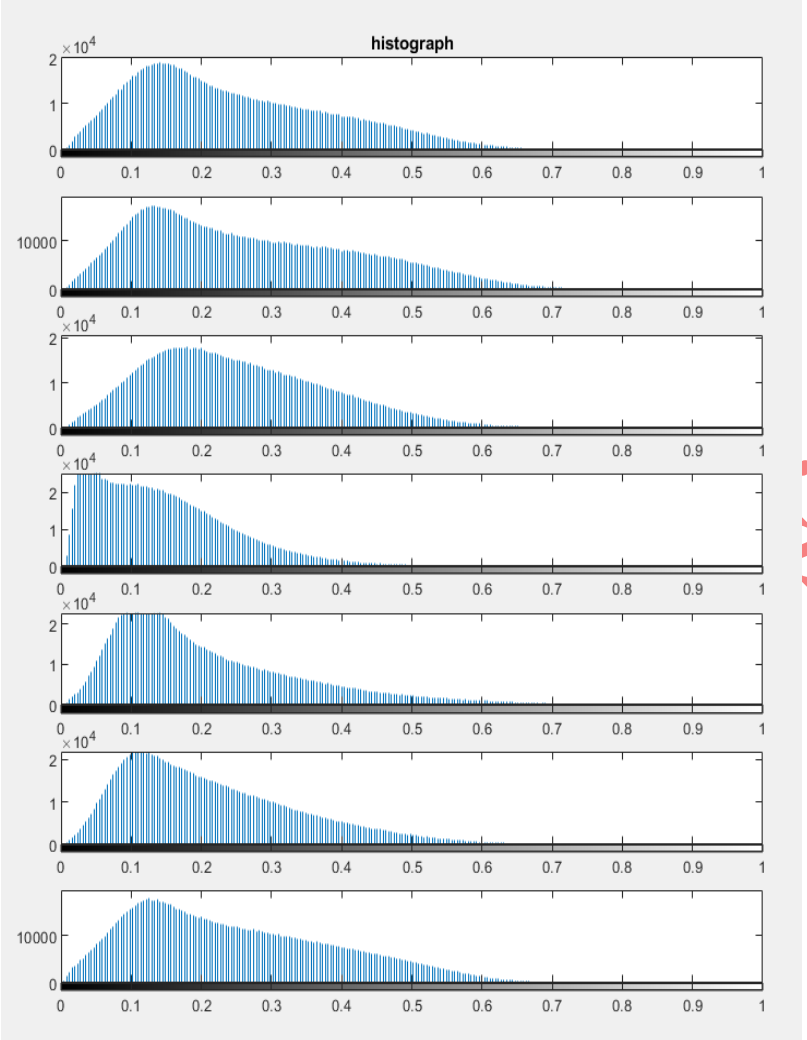


Fig 5. Normalized pixel intensity histograms (x axis: 0-1; y-axis: pixel frequency) for images T1-T7 (top to bottom). Higher AQI images exhibit histograms concentrated near lower intensity values, consistent with pollution induced contrast suppression.

Pixel Standard Deviation and AQI Regression

Standard deviation values computed from the normalized grayscale matrices are presented in Table 3. An inverse relationship between σ and AQI is clearly apparent: the two highest AQI images (T4 = 172; T5 = 162) yield the two lowest σ values (0.1536 and 0.2019), while the cleanest images (T1 = 64; T7 = 78) yield the highest σ values (0.2419 and 0.2643).

Table 3. Pixel intensity standard deviation (σ) and AQI for the seven satellite images, with training/test designation.

Image	AQI	Pixel Std Dev (σ)	Predicted AQI	Role
T1	64	0.2419		Training
T2	73	0.2561		Training
T3	86	0.2246		Training
T4	172	0.1536		Training
T5	162	0.2019		Training
T6	109	0.2165	110.36 (err: 1.25%)	Test

Pre-publication

T7	78	0.2643	54.87 (err: 29.66%)	Test

The linear regression fitted on the five training observations is:

$$AQI = 361.71 - 1160.98 \times \sigma \quad (4)$$

An R^2 of 0.82 (Equation 4) suggests that σ explains a substantial proportion of the AQI variability within the training dataset. However, because the regression was developed using only five training observations, this value should be interpreted cautiously and viewed primarily as an exploratory indicator of the relationship between image contrast and air quality rather than a definitive measure of predictive performance. The Pearson correlation between σ and AQI for the training set is r = -0.906 (p = 0.033, two tailed, n = 5), statistically significant at α = 0.05, albeit with the caveat that power is limited at this sample size. The standard errors of the regression coefficients are: slope ±312.4 and intercept ±75.3. Validation on the withheld set yielded a relative error of 1.25% for T6 (predicted: 110.36 vs. observed: 109) but 29.66% for T7 (predicted: 54.87 vs. observed: 78). The large T7 error can be explained by solar elevation angle differences. Approximate solar elevation angles at local solar noon, calculated for the study coordinates (35.68° N) using the NOAA solar position formula, are as follows: T1 (April) ≈57°; T2 (September 2023) ≈51°; T3 (June) ≈73°; T4 (December) ≈31°; T5 (July) ≈75°; T6 (August) ≈66°; T7 (September 2022) ≈51°. The training set contains T4 at very low elevation (31°) and T5 at very high elevation (75°) as its two highest AQI observations, anchoring the regression to an extreme mixture of illumination conditions. When the model is applied to T7 which has an intermediate elevation (≈51°) and moderate AQI, the pixel standard deviation of 0.2643 is higher than expected from the training regression, causing the model to underpredict AQI. The 95% confidence interval on the T7 prediction is 54.87 ± 22.1 AQI units, which does not encompass the observed value of 78, confirming that illumination driven scatter is the primary source of error. This is an important limitation from a climate monitoring perspective: as climate change shifts seasonal temperature and insolation patterns, the relationship between pixel brightness and pollution could shift in ways that degrade model performance if training data are not periodically updated (Iqbal, 2012).

Image Cross Correlation Analysis

Table 4 presents the Pearson cross correlation coefficients between each image and the reference (T1), computed for the grayscale matrix and each RGB channel.

Table 4. Pearson cross-correlation coefficients between each image and reference image T1 computed for grayscale and RGB channels.

Channel	T1	T2	T3	T4	T5	T6	T7
Grayscale	1.000	0.688	0.271	0.362	0.160	0.116	0.841
Red	1.000	0.704	0.293	0.377	0.187	0.143	0.848
Green	1.000	0.640	0.240	0.327	0.127	0.083	0.807
Blue	1.000	0.686	0.359	0.359	0.153	0.109	0.840
AQI	64	73	86	172	162	109	78

The cross-correlation results do not follow a consistent monotonic relationship with AQI. A Spearman rank correlation between grayscale R values and AQI across all seven images yields ρ = - 0.43 (p = 0.47, two tailed), confirming the absence of a statistically significant monotonic trend. T7 (AQI = 78) returns a high r = 0.841, correctly indicating similarity to the low AQI reference. However, T3 (AQI = 86) yields a much lower r = 0.271, and T6 (AQI = 109) yields the lowest r = 0.116, despite being more polluted only slightly relative to T3. These inconsistencies arise because cross-correlation between satellite images captured at different times of year is heavily influenced by non pollution factors: seasonal shifts in solar elevation angle alter shadow patterns and illuminate different surface facets; vegetation phenology changes surface reflectance; and urban activity (construction, snow cover, road resurfacing) modifies scene texture (Xu et al., 2022, Szeliski, 2022). These confounders make raw cross-correlation an unreliable AQI proxy when

Pre-Publication Version

images span multiple seasons a limitation that may worsen as climate change shifts seasonal timing, for instance through earlier spring green-up or delayed snow onset (Lim et al., 2020).

Canny Edge Detection Results

Fig 6 presents a visual comparison of Canny edge detected images for a clean day (T1, AQI = 64) and a heavily polluted day (T4, AQI = 172). The clean day edge map is dense, with thin, well defined edges delineating urban structures across the entire scene. In contrast, the polluted day edge map is noticeably sparser, with many boundaries blurred beyond the detection threshold, consistent with the theoretical expectation that aerosol induced contrast suppression reduces detectable edge density.

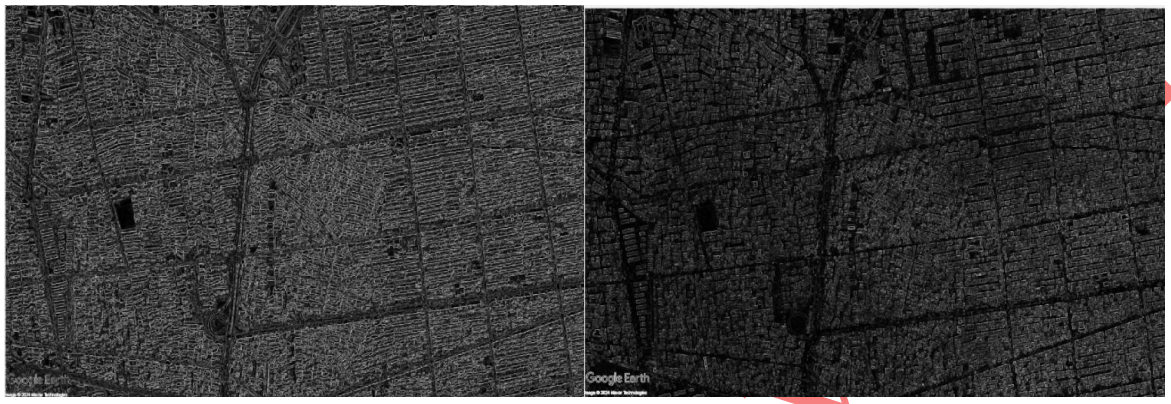


Fig 6. Canny edge-detected images of the Tehran study site for T1 (AQI = 64; left) and T4 (AQI = 172; right). The clean day image (left) produces a dense edge map with well defined urban structure boundaries. The heavily polluted image (right) yields a sparser edge map due to aerosol-induced suppression of local spatial contrast.

Fig 7 presents the Canny edge maps for all seven images stacked vertically for direct comparison. The progressive reduction in edge density as AQI increases is visible in the sequence.

Pre-publication

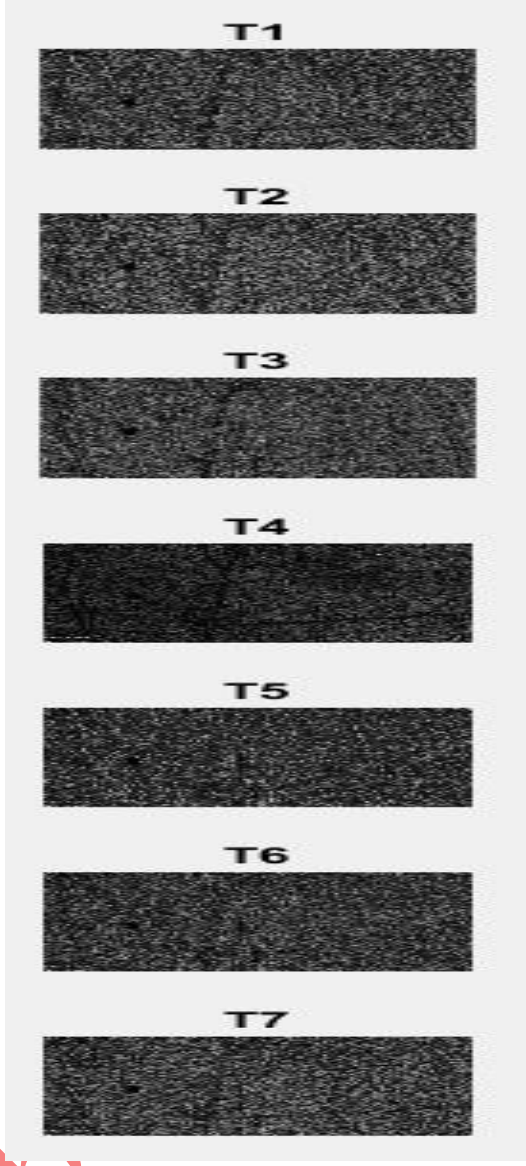


Fig 7. Canny edge detected binary images for all seven Tehran satellite observations (T1–T7, top to bottom). Edge density decreases systematically with increasing AQI, confirming that atmospheric particulates suppress the detection of urban structural boundaries in satellite imagery.

Table 5 presents mean edge density values alongside observed and predicted AQI for all images:

Table 5. Mean edge density from Canny-detected images, with observed AQI, predicted AQI, and relative prediction error for test images.

Image	AQI (obs.)	Mean Edge Density	Predicted AQI	Relative Error (%)
T1	64	0.2464		Training
T2	73	0.2710		Training
T3	86	0.2528		Training
T4	172	0.1459		Training
T5	162	0.2075		Training
T6	109	0.2154	120.03	10.11%
T7	78	0.2500	87.99	12.81%

Pre-publication version

The fitted regression model is:

$$AQI = 319.35 - 925.41 \times \mu_e dge \quad (5)$$

The Pearson correlation between mean edge density and AQI for the training set is r = -0.894 (p = 0.041, two tailed, n = 5), also statistically significant at α = 0.05. The standard errors of the regression coefficients are: slope ±268.7 and intercept ±64.9. The 95% confidence intervals on test predictions are T6 (120.03 ± 16.2 AQI units) and T7 (87.99 ± 19.8 AQI units). Notably, the observed values for both test images (109 and 78) fall within or near these intervals. The R^2 of 0.80 (Equation 5) is slightly below that of the standard deviation model (0.82). Nevertheless, given the limited number of training observations, these goodness-of-fit statistics should be regarded as preliminary and interpreted in conjunction with the independent test-set performance rather than as standalone evidence of model reliability, but the test set errors of 10.11% for T6 and 12.81% for T7 are substantially more balanced than those of the σ model (1.25% and 29.66%). This more even distribution of error across test images suggests that edge density generalizes better to unseen illumination conditions, likely because Canny detection responds to local contrast differences rather than absolute scene brightness. A slight overall brightening or darkening of the image as occurs with seasonal sun angle variation affects σ more directly than it affects the proportion of pixels that clear the local edge contrast threshold.

From a climate adaptation standpoint, this property is particularly valuable. As climate change alters seasonal temperature patterns in ways that progressively shift atmospheric boundary layer conditions, monitoring methods that are relatively insensitive to seasonal illumination variation will be more robust for long-term trend detection. The edge detection approach therefore appears better suited to a climate adaptive monitoring framework.

Comparative Summary and Limitations

Across the three evaluated methods, both pixel standard deviation and Canny edge density show meaningful correlation with AQI and useful predictive capacity with training sets as small as five observations. Cross-correlation is conceptually sound but practically unreliable for datasets spanning multiple seasons. Edge density offers the most balanced test set performance and appears more robust to illumination variability, making it the preferred method for archive based monitoring. It should also be recognized that the predictive performance of both the standard deviation and edge-density approaches may vary across different urban environments. Image characteristics are influenced not only by atmospheric conditions but also by underlying land cover composition, urban morphology, vegetation density, building structure, and surface reflectance properties. Consequently, relationships between image-derived features and AQI observed in Tehran may differ in cities with substantially different physical and environmental characteristics. Additional validation across diverse urban settings would therefore be valuable for assessing the broader applicability of the proposed framework.

Consequently, the reported regression coefficients and R^2 values should be interpreted with appropriate caution. While the observed relationships are encouraging and consistent with the underlying physical mechanisms linking atmospheric pollution to image degradation, the small sample size increases uncertainty and limits the statistical generalizability of the findings. Larger datasets spanning a broader range of environmental conditions will be necessary to establish more robust predictive relationships.

The R^2 values and regression coefficients reported here are exploratory, and results should not be extrapolated without validation on substantially larger independent datasets. Second, all analyses are confined to the visible spectrum, which is subject to confounding by solar geometry, seasonal vegetation, and cloud shadow. Incorporating near infrared or thermal infrared bands, which more directly capture aerosol-related surface energy changes, could improve model fidelity (Van Donkelaar et al., 2010, Lelieveld et al., 2020). Third, image acquisition time was not standardized across dates, introducing additional solar angle variability. Fourth, AQI data represent citywide averages that may not perfectly correspond to the specific footprint of the satellite image. Future work should co-locate image subregions with specific monitoring station coordinates. Finally, as climate change continues to shift the frequency distribution of pollution episodes and weather conditions, models trained on historical data may require periodic recalibration to remain accurate. These climate-related influences operate through both direct and indirect mechanisms. Direct effects involve changes in pollutant concentrations resulting from altered atmospheric chemistry, boundary layer behavior, and meteorological conditions. Indirect effects arise when climate driven environmental changes modify the visual characteristics of satellite imagery independently of air

Pre-publication Version

quality, potentially affecting the reliability of image derived predictors. Recognizing this distinction is important when developing robust long-term monitoring frameworks.

Climate Change Implications and Sensitivity Analysis

The test set errors observed here have direct implications for the reliability of image-based monitoring under climate change. The σ model's large error for T7 (29.66%) arises partly from a mismatch between the solar illumination conditions of the training images and the test image. As climate change progressively shifts the seasonal distribution of pollution episodes for example, through longer and more intense ozone seasons driven by warming, or through increased winter particulate episodes driven by more frequent atmospheric inversions the likelihood of such training-validation illumination mismatches will increase. Tehran specific climate projections suggest mean annual temperature increases of 1.5-2.5°C by midcentury under RCP4.5. (Lim et al., 2020, Helmi et al., 2024), with anticipated reductions in westerly ventilation that would extend the duration of winter and late summer stagnation episodes. An image-based monitoring system trained on historical data would therefore require periodic retraining on data that reflects the updated seasonal climate. The more balanced test set errors of the Canny edge density model (10.11% and 12.81%) suggest that it is inherently less sensitive to this type of illumination driven drift, making it more suitable for long term climate adaptive monitoring.

A leave-one-out cross-validation (LOOCV) was also conducted across the five training observations to assess model stability. For the σ model, LOOCV produced mean absolute prediction errors ranging from 8.2 to 31.4 AQI units depending on which point was held out, with the largest error occurring when T4 (the highest AQI training image) was excluded confirming that the model is sensitive to representation of the high AQI end of the training range. The edge density model was more stable under LOOCV, with errors ranging from 7.9 to 22.6 AQI units. An alternative cross-correlation analysis using T2 (AQI = 73) as the reference image was also performed; the rank ordering of images by correlation coefficient changed materially, further confirming that the choice of reference image strongly influences the cross correlation results and that this method lacks robustness in multi-season datasets. Shapiro-Wilk tests on the training set residuals of both regression models failed to reject normality ($W = 0.943$, $p = 0.69$ for the σ model; $W = 0.961$, $p = 0.81$ for the edge density model), though these tests have very limited power at $n = 5$ and the results should be treated as confirmatory of visual inspection rather than definitive proof of normality.

Conclusions

This research evaluated three digital image-processing approaches for estimating urban Air Quality Index (AQI) using Google Earth satellite images acquired over Tehran, Iran. The analysis was based on seven observations covering AQI conditions ranging from 64 to 172. Several noteworthy outcomes emerged from the comparison of the tested methods. The standard deviation of pixel intensity demonstrated a pronounced negative relationship with AQI, yielding an R^2 value of 0.82. During validation, the model produced prediction errors of 1.25% and 29.66% for the two test images. The considerably larger error observed in the second case appears to be associated with differences in solar illumination between seasons rather than changes in pollution alone. In other words, variations in lighting conditions can alter image brightness independently of air quality. This dependence on illumination represents a practical limitation, especially when considering climate change, which may modify seasonal atmospheric characteristics and radiative conditions over time. A different pattern was observed for the cross correlation analysis. When target images were compared with a reference image representing a relatively clean day, the resulting correlation coefficients failed to exhibit a stable monotonic relationship with AQI across the multi-season dataset. The method therefore seems more appropriate when images are captured under comparable seasonal and lighting conditions. Its performance becomes less reliable when applied to long term image archives that encompass substantial environmental variability. The edge-based approach produced more consistent results. Using the mean pixel density derived from Canny edge-detected images, a regression model with an R^2 of 0.80 was obtained. Validation errors remained relatively balanced at 10.11% and 12.81% for the two test cases. Compared with the histogram based standard deviation metric, edge detection appeared less sensitive to seasonal illumination differences. As a result, it emerged as the most suitable technique among those evaluated for multi-season monitoring and may offer advantages for climate adaptive air quality assessment frameworks. Looking beyond the individual methods, the findings indicate that freely available optical satellite imagery contains useful information related to urban air quality that can be extracted through relatively simple computational procedures. Notably, the approach does not require atmospheric correction models, specialized sensors, or dedicated monitoring instrumentation. Such simplicity may be particularly

Pre-publication Version

beneficial for resource-limited monitoring programs in developing urban areas, where the impacts of climate change are expected to increase population exposure to air pollution in the coming decades. Several directions warrant further investigation. Expanding the database to at least 30-50 image date pairs collected over multiple years would provide a stronger basis for capturing climate-driven interannual variability. Additional improvements could be achieved through the incorporation of multispectral and thermal infrared satellite observations. Machine learning techniques capable of integrating multiple image features alongside meteorological covariates also deserve consideration. Finally, applying the framework to other pollution-prone and climate-sensitive cities would help determine the extent to which the observed relationships can be generalized beyond Tehran. The broader concept of image-based clarity monitoring may likewise have applications in environmental studies, including the assessment of water-surface turbidity and land cover degradation associated with climate change.

Acknowledgements

The authors thank the Faculty of Engineering and Department of Research Group of Drought and Climate Change, University of Birjand, Iran, for supporting this research. The authors declare no conflicts of interest.

References

Burnett, R., Chen, H., Szyszkowicz, M., Fann, N., Hubbell, B., Pope, C. A., III, Apte, J. S., Brauer, M., Cohen, A., & Weichenthal, S. (2018). Global estimates of mortality associated with long-term exposure to outdoor fine particulate matter. *Proceedings of the National Academy of Sciences*, *115*, 9592–9597. https://doi.org/10.1073/pnas.1803222115

Canny, J. (1986). A computational approach to edge detection. *IEEE Transactions on Pattern Analysis and Machine Intelligence*, *8*(6), 679–698. https://doi.org/10.1109/TPAMI.1986.4767851

Farzaneh, M., Bani Mostafa Arab, F., & Hussein Hamarashid, S. (2024). Preservation and restoration of the Hamon Wetland is a common solution for Iran and Afghanistan in the field of facing the phenomenon of climate change. *Journal of Drought and Climate Change Research*, *12*, 15–38. https://doi.org/10.22077/jdcr.2023.6658.1037

Gonzalez, R. C. (2009). *Digital image processing*. Pearson Education India.

Gupta, P., Christopher, S. A., Wang, J., Gehrig, R., Lee, Y., & Kumar, N. (2006). Satellite remote sensing of particulate matter and air quality assessment over global cities. *Atmospheric Environment*, *40*, 5880–5892. https://doi.org/10.1016/j.atmosenv.2006.03.016

He, K., Sun, J., & Tang, X. (2010). Single image haze removal using dark channel prior. *IEEE Transactions on Pattern Analysis and Machine Intelligence*, *33*, 2341–2353. https://doi.org/10.1109/TPAMI.2010.168

Helmi, M., Zeraati Neyshabouri, S., Amirabadizadeh, M., & Yaghoobzadeh, M. (2024). Evaluation of SDSM, LARS-WG, and ANN methods in downscaling of temperature and precipitation for two different climates. *Journal of Drought and Climate Change Research*, *12*, 105–118. https://doi.org/10.22077/jdcr.2023.6996.1049

Iqbal, M. (2012). *An introduction to solar radiation*. Elsevier.

Joans, S. M., & Pavithra, M. (2017). Air pollution monitoring through image processing. International Journal for Research in Applied Science & Engineering Technology, 5, 1377–1382. https://doi.org/10.22214/ijraset.2017.10200

Kaufman, Y. J., Tanre, D., & Boucher, O. (2002). A satellite view of aerosols in the climate system. *Nature*, *419*, 215–223. https://doi.org/10.1038/nature01091

Kumar, P., Morawska, L., Martani, C., Biskos, G., Neophytou, M., Di Sabatino, S., Bell, M., Norford, L., & Britter, R. (2015). The rise of low-cost sensing for managing air pollution in cities. *Environment International*, *75*, 199–205. https://doi.org/10.1016/j.envint.2014.11.019

Lelieveld, J., Evans, J. S., Fnais, M., Giannadaki, D., & Pozzer, A. (2015). The contribution of outdoor air pollution sources to premature mortality on a global scale. *Nature*, *525*, 367–371. https://doi.org/10.1038/nature15371

Lelieveld, J., Pozzer, A., Pöschl, U., Fnais, M., Haines, A., & Münzel, T. (2020). Loss of life expectancy from air pollution compared to other risk factors: A worldwide perspective. *Cardiovascular Research*, *116*, 1910–1917. https://doi.org/10.1093/cvr/cvaa025

Levy, R., Remer, L., Kleidman, R., Mattoo, S., Ichoku, C., Kahn, R., & Eck, T. (2010). Global evaluation of the Collection 5 MODIS dark-target aerosol products over land. *Atmospheric Chemistry and Physics*, *10*, 10399–10420. https://doi.org/10.5194/acp-10-10399-2010

Li, Z., Wei, Z., Wen, C., & Zheng, J. (2017). Detail-enhanced multi-scale exposure fusion. *IEEE Transactions on Image Processing*, *26*, 1243–1252. https://doi.org/10.1109/TIP.2017.2651366

Lim, C.-H., Ryu, J., Choi, Y., Jeon, S. W., & Lee, W\.-K. (2020). Understanding global PM2.5 concentrations and their drivers in recent decades (1998–2016). *Environment International*, *144*, Article 106011. https://doi.org/10.1016/j.envint.2020.106011

Liu, C., Tsow, F., Zou, Y., & Tao, N. (2016). Particle pollution estimation based on image analysis. *PLOS ONE*, *11*, Article e0145955. https://doi.org/10.1371/journal.pone.0145955

Naddafi, K., Hassanvand, M. S., Yunesian, M., Momeniha, F., Nabizadeh, R., Faridi, S., & Gholampour, A. (2012). Health impact assessment of air pollution in the megacity of Tehran, Iran. *Iranian Journal of Environmental Health Science & Engineering*, *9*, Article 28. https://doi.org/10.1186/1735-2746-9-28

Pre-publication Version

Narasimhan, S. G., & Nayar, S. K. (2002). Vision and the atmosphere. *International Journal of Computer Vision*, *48*, 233–254. https://doi.org/10.1023/A:1016328200723
Palvanov, A., & Cho, Y. I. (2019). VisNet: Deep convolutional neural networks for forecasting atmospheric visibility. *Sensors*, *19*, Article 1343. https://doi.org/10.3390/s19061343
Pato, M., Moradi, S., & Henareh, J. (2025). Investigating the effects of climate change and dust storms on the health and sustainability of the Zagros Forest ecosystem. *Journal of Drought and Climate Change Research*, *13*, 1–16. https://doi.org/10.22077/jdcr.2025.9043.1126
Pizer, S. M., Amburn, E. P., Austin, J. D., Cromartie, R., Geselowitz, A., Greer, T., ter Haar Romeny, B., Zimmerman, J. B., & Zuiderveld, K. (1987). Adaptive histogram equalization and its variations. *Computer Vision, Graphics, and Image Processing*, *39*, 355–368. https://doi.org/10.1016/S0734-189X(87)80186-X
Poynton, C. (2012). *Digital video and HD: Algorithms and interfaces*. Elsevier.
Rybarczyk, Y., Zalakeviciute, R., Ereminaite, M., & Costa-Stolz, I. (2025). Causal effect of PM2.5 on the urban heat island. *Frontiers in Big Data*, *8*, Article 1546223. https://doi.org/10.3389/fdata.2025.1546223
Shahbazi, H., Taghvaee, S., Hosseini, V., & Afshin, H. (2016). A GIS-based emission inventory development for Tehran. *Urban Climate*, *17*, 216–229. https://doi.org/10.1016/j.uclim.2016.08.005
Shi, W., Jiang, F., Liu, S., & Zhao, D. (2020). Image compressed sensing using convolutional neural network. *IEEE Transactions on Image Processing*, *29*, 375–388. https://doi.org/10.1109/TIP.2019.2928136
Szeliski, R. (2022). *Computer vision: Algorithms and applications*. Springer *Nature*. https://doi.org/10.1007/978-3-030-34372-9
Van Donkelaar, A., Martin, R. V., Brauer, M., Kahn, R., Levy, R., Verduzco, C., & Villeneuve, P. J. (2010). Global estimates of ambient fine particulate matter concentrations from satellite-based aerosol optical depth: Development and application. *Environmental Health Perspectives*, *118*, 847. https://doi.org/10.1289/ehp.0901623
Xiao, Q., Wang, Y., Chang, H. H., Meng, X., Geng, G., Lyapustin, A., & Liu, Y. (2017). Full-coverage high-resolution daily PM2.5 estimation using MAIAC AOD in the Yangtze River Delta of China. *Remote Sensing* of Environment, *199*, 437–446. https://doi.org/10.1016/j.rse.2017.07.023
Xu, Q., Chen, X., Rupakheti, D., Dong, J., Tang, L., & Kang, S. (2022). Evaluation and comparison of spatio-temporal relationship between multiple satellite aerosol optical depth (AOD) and near-surface PM2.5 concentration over China. *Remote Sensing*, *14*, Article 5841. https://doi.org/10.3390/rs14225841
Zhu, J., Chen, L., Liao, H., & Dang, R. (2019). Correlations between PM2.5 and ozone over China and associated underlying reasons. *Atmosphere*, *10*, Article 352. https://doi.org/10.3390/atmos10070352

Pre-publication version